Quantum-Mechanical Prediction of Nanoscale Photovoltaics

Yu Zhang,[†] LingYi Meng,[‡,†] ChiYung Yam,[§,†] and GuanHua Chen*[,†]

[†]Department of Chemistry, The University of Hong Kong, Pokfulam Road, Hong Kong, China
[‡]Collaborative Innovation Center of Chemistry for Energy Materials, Xiamen University, Xiamen 361005, China
[§]Beijing Computational Science Research Center, No. 3 He-Qing Road, Beijing 100084, China

ABSTRACT: Previous simulations of photovoltaic devices are based on classical models, which neglect the atomistic details and quantum-mechanical effects besides the dependence on many empirical parameters. Here, within the nonequilibrium Green's function formalism, we present a quantum-mechanical study of the performance of inorganic nanowire-based photovoltaic devices. On the basis of density-functional tight-binding theory, the method allows simulation of current–voltage characteristics and optical properties of photovoltaic devices without relying on empirical parameters. Numerical studies of silicon nanowire-based devices of realistic sizes with 10 000 atoms are performed, and the results indicate that atomistic details and nonequilibrium conditions have a clear impact on the photoresponse of the devices.
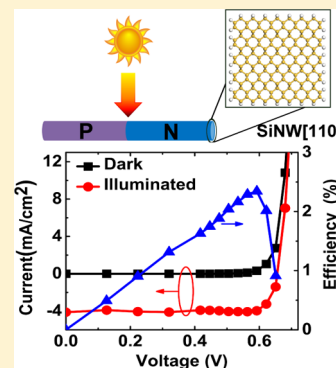
SECTION: Energy Conversion and Storage; Energy and Charge Transport

The increasing demand of renewable energy supply motivates the searching for high-efficiency photovoltaic devices.[1−9] Semiconductor nanostructured photovoltaic devices are a new generation of devices with high power conversion efficiencies (PCEs). Recent studies found that the nanowire-based solar cell is able to achieve high PCE, which breaks the traditional limit.[1,2] To increase the efficiency of solar cells, detailed knowledge of electron−hole generation upon photon absorption and charge transport is required. Unfortunately, on the nanoscale, theoretical prediction of performance of solar cells is a formidable task. The main challenge comes from the fact that the optical and electronic properties of the nanoscale structures need to be described at a high level of accuracy, and the atomistic details have important effects on the performance of devices. However, the majority of previous theoretical methods are based on classical models (e.g., the dynamic Monte Carlo approach[10,11] and the drift-diffusion model[12−14]), which fail to describe such devices with atomistic details and quantum effects. Besides, the classical models rely on many empirical parameters, such as electron−hole generation (recombination) rate and electron (hole) mobilities.[12−14] It is desirable to develop a quantum-mechanical microscopic quantum theory for the description of nanoscale photovoltaic devices. In our previous work, we developed a density-functional tight-binding (DFTB)-based[15] nonequilibrium Green's function (NEGF)[16−18] method to model electrical response of nanoelectronic devices.[19] Here the DFTB-NEGF method is extended to include electron−photon interaction and is applied to study the performance of novel nanoscale photovoltaic devices.

The system we considered here is a two-terminal photovoltaic device with PN junction, which is formed by p-type doping on one side and n-type doping on the other side. A linearly polarized light is applied to the system, and it is assumed that only the device region is illuminated. Hamiltonian adopts Coulomb gauge and is expressed as[20−22]

$$H = \frac{1}{2m}(\boldsymbol{p} + e\boldsymbol{A})^2 + V(\boldsymbol{r}) = H_e + \frac{e}{m}\boldsymbol{A}\cdot\boldsymbol{p} + \frac{e^2}{2m}\boldsymbol{A}^2 \tag{1}$$

where H_e employs the DFTB Hamiltonian without electric field, which allows for an efficient construction of Kohn−Sham (KS) Fock matrix, $\boldsymbol{A}$ is the time-dependent electromagnetic vector potential, $\boldsymbol{p}$ is the electronic momentum operator, e is the elementary charge, and m is the electron mass. The last two terms in the previous equation can be expressed as H_{er} and H_r, which represent the electron−photon interaction Hamiltonian and photon Hamiltonian, respectively. H_{er} describes the coupling between light and electron. It describes the photocurrent generation and radiative recombination process. In general, the vector potential $\boldsymbol{A}$ has spatial dependence, that is, $\boldsymbol{A}(\boldsymbol{r})$. However, the photovoltaic devices considered in this work are on the nanoscale, which is much smaller compared with the wavelength of the electric field. The dipole approximation is thus used where the spatial resolution of radiation field is neglected.

Under the dipole approximation, the second quantized vector potential reads

$$A(t) = a\left(\frac{\hbar\sqrt{\tilde{\mu}\tilde{\varepsilon}}}{2N\omega\epsilon c}F_r\right)^{1/2}(be^{-i\omega t} + b^{\dagger}e^{i\omega t}) \tag{2}$$

where $\tilde{\mu}$ and $\tilde{\varepsilon}$ are relative magnetic and dielectric constants, respectively; ϵ is the dielectric constant and $\hbar$ is the reduced Planck constant; c is the light speed; N is the number of photons determined by the Bose−Einstein distribution function; ω is the frequency of photon, and F_r is the corresponding photon flux, which is defined as the number of photon per unit time per unit area. a is the direction of A determined by the polarization of the field. b and $b^{\dagger}$ are the annihilation and creation operators of photon, respectively. Within second quantization formalism, H_{er} can be expressed in terms of annihilation and creation operators in certain basis. In the atomic basis set, this interaction Hamiltonian H_{er} is rewritten as

$$H_{er} = \sum_{\mu\nu}\langle\mu|H_{er}|\nu\rangle d_{\mu}^{\dagger}d_{\nu} = \sum_{\mu\nu}\frac{e}{m}A\cdot\langle\mu|p|\nu\rangle d_{\mu}^{\dagger}d_{\nu} \tag{3}$$

where d_{ν} and $d_{\mu}^{\dagger}$ are the corresponding annihilation and creation operators of electron. The last equality in the above equation is satisfied because the vector potential A is spatially independent under the dipole approximation. Substituting eq 2 into the previous equation, we obtain the expression of interaction Hamiltonian H_{er} as

$$H_{er} = \sum_{\mu\nu}e\left(\frac{\hbar\sqrt{\tilde{\mu}\tilde{\varepsilon}}}{2N\omega\epsilon c}F_r\right)^{1/2}(be^{-i\omega t} + b^{\dagger}e^{i\omega t})a\cdot\langle\mu|\frac{p}{m}|\nu\rangle d_{\mu}^{\dagger}d_{\nu}$$
$$\equiv \sum_{\mu\nu}M_{\mu\nu}(be^{-i\omega t} + b^{\dagger}e^{i\omega t})d_{\mu}^{\dagger}d_{\nu} \tag{4}$$

where M is the electron−photon coupling matrix. This interaction Hamiltonian is similar to that of electron−phonon coupling. Because both photons and phonons are bosons and subject to Bose−Einstein statistics, their interactions with electrons have similar properties. Thus, following the same procedure in ref 23, the lesser and greater self-energies, $\sum_{er}^{<}(E)$ and $\sum_{er}^{>}(E)$, due to electron−photon interaction, can be expressed as

$$\Sigma_{er}^{<,>}(E) = M[NG^{<,>}(E \mp \hbar\omega) + (N+1)G^{<,>}(E \pm \hbar\omega)]M \tag{5}$$

where $G^{<}(E)$ and $G^{>}(E)$ are the lesser and greater electron Green's functions, respectively. It is noted that eq 5 is nonlinear due to the fact that self-energies are dependent on Green's functions. Green's functions and self-energies, in principle, have to be calculated self-consistently. The number of iterations depends on the electric field strength. In cases of strong field, more iterations are expected in the self-consistent calculations, while convergence can be readily achieved in a few steps when the system is only weakly perturbed by the external field. Similar to that in ref 23, the lowest order expansion to the self-energy $\sum_{er}^{<,>}(E)$ is employed in this work. This is justified by the fact that the intensity of light is not strong and the typical electron−photon interaction in the photovoltaic devices is small. Therefore, the nonlinear effects are not as important and are neglected. First, a self-consistent solution of Hamiltonian and charge density is obtained for the device without the electron−photon interaction.[19] This is done by solving the Poisson equation within NEGF formalism. The bare Green's

functions, $G_0^{<,>}(E)$, are then used to construct the self-energy $\sum_{er}^{<,>}(E)$ and device Green's function including the electron−photon interaction, that is

$$\Sigma_{er}^{<,>}(E) = M[NG_0^{<,>}(E \mp \hbar\omega) + (N+1)G_0^{<,>}$$
$$(E \pm \hbar\omega)]M \tag{6}$$

and the electron Green's function at the lowest order with respect to the electron-photon coupling reads

$$G^{<}(E) = G_0^r(E)[i\sum_{\alpha}f_{\alpha}(E)\Gamma_{\alpha}(E) + \Sigma_{er}^{<}(E)]G_0^a(E) \tag{7}$$

where $\Gamma_{\alpha}(E)$ is the line-width function due to coupling between device and lead α; $f_{\alpha}(E)$ is the Fermi−Dirac distribution function of lead α;[23] $G_0^r(E)$ and $G_0^a(E)$ are the retarded and advanced Green's functions, respectively. Then, the resulting Green's function and self-energy are used to evaluate the current. Expression of current within NEGF formalism is[24]

$$I_{\alpha} = \frac{2e}{\hbar}\int\frac{dE}{2\pi}Tr[\Sigma_{\alpha}^{<}(E)G^{>}(E) - \Sigma_{\alpha}^{>}(E)G^{<}(E)] \tag{8}$$

where the factor of two arises from the spin degeneracy. Substituting eq 7 into the above equation gives the expression of the current I_{α}, which can be divided into two terms. The first term is the elastic part, which is

$$I_{\alpha}^{el} = \frac{2e}{\hbar}\sum_{\beta\neq\alpha}\int\frac{dE}{2\pi}[f_{\alpha}(E) - f_{\beta}(E)]T(E) \tag{9}$$

where $T(E) = Tr[\Gamma_{\alpha}(E)G_0^r(E)\Gamma_{\beta}(E)G_0^a(E)]$ is the transmission coefficient. I_{α}^{el} is same as the expression of current for noninteracting systems.[24] The second term of the expression of current I_{α} is the inelastic part, which is expressed as

$$I_{\alpha}^{inel} = \frac{2e}{\hbar}\int\frac{dE}{2\pi}Tr\{\Gamma_{\alpha}(E)G_0^r(E)\Gamma_{eff}(E)G_0^a(E)\}$$
$$\equiv \frac{2e}{\hbar}\int\frac{dE}{2\pi}T_{inel}(E) \tag{10}$$

where $T_{inel}(E)$ is defined as the inelastic transmission and $\Gamma_{eff}(E) = i\{f_{\alpha}(E)\sum_{er}^{>}(E) - [f_{\alpha}(E) - 1]\sum_{er}^{<}(E)\}$ can be regarded as the Fermi-weighted self-energy. The expression of I_{α}^{inel} is similar to that of I_{α}^{el} except that the Fermi function is absorbed into the Fermi-weighted self-energy $\Gamma_{eff}(E)$. I_{α}^{inel} represents the photon-induced current, that is, the photocurrent. Because the electron-photon coupling matrix M is proportional to $F_r^{1/2}$, the photocurrent is then proportional to the incident photon flux F_r at lowest order expansion to self-energy. Optical-induced transitions between valence and conduction bands are accompanied by photon absorption, which means that the electric current associated with this transition accounts for the corresponding photon absorption.[25,26] After some algebra, the absorption flux F_a can be derived as

$$F_a(\omega) = \frac{2}{\hbar}\int\frac{dE}{2\pi}TrN[MG_0^>(E)MG_0^<(E - \hbar\omega)$$
$$- MG_0^<(E)MG_0^>(E - \hbar\omega)] \tag{11}$$

Thus, absorptivity $\alpha(\omega)$ is evaluated through F_a/F_r. $\alpha(\omega)$ can also be derived from the current−current correlation function, which is given by Kubo−Greenwood formula.[27] With the absorption flux, internal quantum efficiency (IQE), which is defined as the ratio of the number of electrons collected by the

photovoltaic device to the number of photons absorbed, can be obtained.

In the numerical implementation, recursive Green's function (RGF) method is adopted to reduce computational complexity and memory usage,[28] which enables quantum-mechanical simulation of realistic systems containing more than 10 000 atoms. There has been experimental evidence showing that coherent length of electron−hole pairs in nanowires can be much longer even at room temperature due to reduced backscattering.[29] Thus, the electron−phonon coupling and its decoherence effect are neglected to reduce the computational costs.

Two silicon nanowires (SiNWs)-based PN junctions are investigated, with cross section of 2×2 nm^2 (NW-A) and 3×3 nm^2 (NW-B), containing 6656 atoms and 12 672 atoms in total, respectively. Both SiNWs are 25 nm long and are oriented in the [110] direction, which is the most common growth orientation for small naowires.[30] The surface of SiNW is terminated by hydrogen to eliminate dangling bond. The SiNWs are doped by Ga/As atoms to generate p/n-type doping at two sides, resulting in a heterojunction. There are four dopants for each type in the SiNWs, corresponding to 8.0×10^{19} cm^{-3} doping concentration for each type in NW-A and 3.56×10^{19} cm^{-3} in NW-B. Temperature $T = 300$ K is used, and the power of incident light is fixed at 1 kW/m^2 throughout the simulation.

Figure 1 plots the local density of states (LDOS) of the NW-A PN junction with 0.0 and 0.6 V forward bias voltage. The left
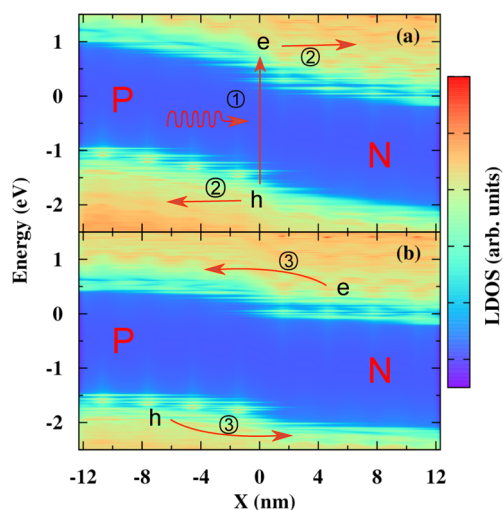

Figure 1. Local density of states of the NW-A with forward bias voltage of (a) 0 and (b) 0.6 V. The bands bend at the interface $X = 0$ and form the built-in voltage across the junction. Forward bias voltage pushes down the bands of p-type SiNW and turns on the PN junction. ① is the electron−hole generation by photon excitation; ② is the electron/hole transport process driven by the build-in potential after the photon excitation; and ③ is the electron/hole transport process of dark current in PN junction under forward bias voltage that occurs as a result of reduction of barrier under forward bias voltage.

side of SiNW is p-doped and the right side is n-doped. Figure 1 shows the density of states distributions in both energy and real spaces. The positions of dopants can also be clearly visualized in the LDOS plot. It is found that the dopant states appear inside the band gap of the SiNW. For the p-type SiNW, the states of dopants are slightly above the valence band of silicon, while the states of dopants are slightly below the conduction

band of silicon for the n-type SiNW. Upon connection of p-doped and n-doped SiNW, both the valence and conduction bands bend and a potential difference is formed, giving rise to the built-in potential across the junction. The built-in potentials of about 1.13 and 1.10 V are observed at the interface for NW-A and NW-B, respectively. When PN junction is illuminated by light, an electron−hole pair is generated after absorbing a photon. The electron flows from the p-type region to the n-type region, owing to the built-in potential, while the hole transports in the opposite direction, resulting in a photocurrent generated in the PN junction. The direction of photocurrent is opposite to the dark current, where electrons flow from n-type region to p-type region in the PN junction.

When forward bias is applied to the SiNW, the potential difference across the junction is reduced. Figure 1b shows the LDOS of NW-A with forward bias voltage 0.6 V. It is found that the energy barrier for electron is largely reduced compared with Figure 1a. Hence, when the forward bias voltage increases, dark current increases as a result of energy barrier reduction. When the forward bias voltage equals to the open-circuit voltage, the dark current eventually offsets the photogenerated current.[10]

Figure 2 shows the $I-V$ curves of the SiNW solar cells. The black lines are dark currents, that is, the currents without light
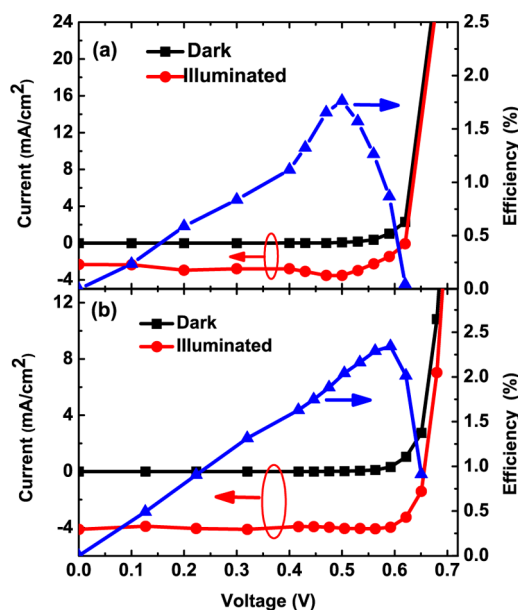

Figure 2. $I-V$ curves of (a) NW-A and (b) NW-B with/without light illumination. Monochromatic light is chosen with photon energy 2.5 eV, which is slightly larger than the VC band gap. Black lines show the dark currents of PN junction. Red lines present the overall $I-V$ characteristics of the SiNW solar cells. Blue lines plot the PCEs of the SiNW solar cells.

illumination; the red lines are the illuminated currents under monochromatic light illumination; the blue lines plot the PCEs (defined as the maximum output power divided by the incident power of photon). The photon energy is chosen to be 2.5 eV, which is slightly larger than the valence-conduction (VC) band gap (2.2 eV for NW-A and 2.0 eV for NW-B). The VC band gap is defined as the energy difference between the conduction band minimum of n-type SiNW and the valence band maximum of p-type SiNW. The power of incident light 1 kW/m^2 corresponds to 2.5×10^{21} m^{-2} s^{-1} photon flux for this

photon energy. The calculated short-circuit currents of NW-A and NW-B are 2.33 and 4.19 mA/cm^2, respectively, and the open-circuit voltages of NW-A and NW-B are 0.62 and 0.66 V, respectively. The current density is obtained through dividing current by the projected area, that is, the area of SiNW under light illumination, for instance, 2×25 nm^2 for the NW-A. It is noted that the simulated open-circuit voltages of the SiNW solar cells are lower than those of conventional photovoltaic devices, which can be close to the built-in voltage. This is attributed to the tunneling dark current, which is significantly larger in these nanostructures. The high doping concentration results in a shortened depletion layer, leading to enhanced tunneling current through the energy barrier before the flat band condition is reached, leading to a lower open-circuit voltage. This also explains the lower open-circuit voltage in NW-A compared with NW-B, owing to the higher doping concentration in NW-A. In experiment, an intrinsic layer can be introduced into the depletion region to reduce the tunneling current.[31]

Using eq 11 and the incident photon flux, we evaluated the absorptivity of the SiNWs. The calculated absorptivity of photon in NW-A is $\alpha_A = 6.5\%$. The low absorptivity can be attributed to the small cross section of the studied nanowire, which is significantly smaller than the penetration depth of silicon. For comparison, the absorptivity of photon in NW-B is $\alpha_B = 12.4\%$, which is larger than α_A as a result of larger absorption depth. Experimentally, the absorptivity can be enhanced by antireflection and light-trapping techniques.[32−34] Considering the absorptivity of photon, the maximum photocurrents that NW-A and NW-B can generate are 2.58 and 4.97 mA/cm^2, respectively, given by the following expression

$$I_{\text{max}}(\omega) = \frac{eP_{\text{in}}}{\hbar\omega}\alpha(\omega) \qquad (12)$$

where P_{in} is the power of the incident light. Hence, the IQEs of the NW-A and NW-B are 90.4 and 84.1%, respectively. The IQEs are <100% due to electron−hole recombination. This recombination loss can be observed in the inelastic transmission $T_{\text{inel}}(E)$, which corresponds to positive values in the inelastic transmission, while the electron−hole generation corresponds to negative values. The difference between the IQEs of the two SiNWs is caused by their different VC band gaps. Because of the lower VC band gap, the monochromatic light in the current study excites electrons in NW-B to higher energies with respect to the conduction band edge. The higher DOS gives rise to a higher recombination rate and results in a lower IQE.

In Figure 2, it is noted that the illuminated currents vary before the kink point, especially in NW-A. This is caused by the change of the electronic structure under nonequilibrium condition, which affects the absorption of photon in return. In contrast with the classical models where the electronic structure far from equilibrium and voltage-dependent photon absorption are neglected, the optical properties of the SiNWs and hence the illuminated currents are changed upon the applied bias voltage. This can be regarded as a fingerprint of the nonequilibrium effect on the photocurrent, which is out of the scope of previous classical descriptions.[10−14] This demonstrates the needs of microscopic quantum-mechanical method for correct description of photovoltaic devices.

Figure 3 gives the short-circuit currents with respect to photon energy. When the photon energy is smaller than the VC
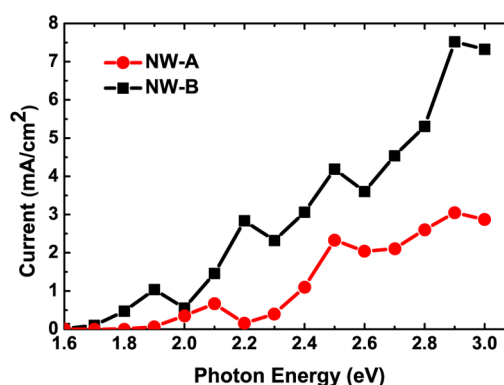

Figure 3. Short-circuit currents with respect to photon energy. The VC gaps of NW-A and NW-B are 2.2 and 2.0 eV, respectively. The nonvanishing short-circuit currents in the energy range below the gaps arise from dopant states within the gap.

band gap, there is almost no photocurrent because photon does not have enough energy to generate electron−hole pair. The simulation results show an onset of photocurrents at 1.9 (NW-A) and 1.7 eV (NW-B), which is lower than the corresponding VC band gaps. Because there are dopant states in the VC band gap, as indicated by Figure 1, photon with energy matching the energy difference between the n-dopant states and p-dopant states can excite electrons from p-dopant states to n-dopant states. Consequently, photocurrent is generated. This phenomenon cannot be observed in classical models, where the dopants are usually considered as an average effect distributed evenly over the host material. Hence, the photocurrent observed in the energy range below the VC band gap is the manifestation of atomistic details of the nanoscale device. It indicates the importance of considering atomistic details. When the photon energy is larger than the gap, photon can be absorbed in a wide range. As a result, the short-circuit current increases with the photon energy as a general trend except small fluctuation. Because the density of states varies in the energy space, photocurrent is suppressed if the photon excitation of electron from valence band to conduction band meets low density of states, resulting in the fluctuation in the short-circuit current.

With the experiment realization of single nanowire photo-voltaics,[31] much effort has been devoted to study the performance of nanowire-based photovoltaic devices. Also, the area of molecular optoelectronics has gained much attention recently.[35] The interactions of these devices with light can be described by the quantum-mechanical method for nanoscale photovoltaic devices presented in this work. The method can also be extended to study the thin-film devices by incorporating 2-D periodic boundary condition with k-point sampling along the thin-film plane. Moreover, applications of this method are not limited to photovoltaic devices; it can also be used to investigate nanoscale optoelectronics and related nanoelectronics, such as photodetectors and photosensors.[36,37] In nanostructured materials, atomistic details, quantum effects, such as confinement, and interference effects are playing important roles in determining the overall performance. The quantum-mechanical method presented in this work provides an efficient research tool for theoretical studies of these nanoscale optoelectronic materials and devices. Recently, a hybrid method that combines quantum mechanics (QM) and electromagnetics (EM), the QM/EM method, has been developed to investigate the interaction between charge and electromagnetic field in novel electronic devices.[38−40] By

Letter

incorporating the current quantum mechanical formalism, the multiscale QM/EM method could be applied to effectively evaluate the performance of photovoltaic devices of more realistic dimensions.

AUTHOR INFORMATION

Corresponding Author

*E-mail: ghc@everest.hku.hk.

Notes

The authors declare no competing financial interest.

REFERENCES

(1) Wallentin, J.; Anttu, N.; Asoli, D.; Huffman, M.; Åberg, I.; Magnusson, M. H.; Siefer, G.; Fuss-Kailuweit, P.; Dimroth, F.; Witzigmann, B.; et al. InP Nanowire Array Solar Cells Achieving 13.8% Efficiency by Exceeding the Ray Optics Limit. *Science* **2013**, *339*, 1057−1060.

(2) Krogstrup, P.; Jorgensen, H. I.; Heiss, M.; Demichel, O.; Holm, J. V.; Aagesen, M.; Nygard, J.; Fontcuberta i Morral, A. Single-Nanowire Solar Cells Beyond the Shockley-Queisser Limit. *Nat. Photon.* **2013**, *6*, 306−310.

(3) Amer, M. R.; Chang, S.-W.; Dhall, R.; Qiu, J.; Cronin, S. B. Zener Tunneling and Photocurrent Generation in Quasi-Metallic Carbon Nanotube pn-Devices. *Nano Lett.* **2013**, *13*, 5129−5134.

(4) Wadhwa, P.; Liu, B.; McCarthy, M. A.; Wu, Z.; Rinzler, A. G. Electronic Junction Control in a Nanotube-Semiconductor Schottky Junction Solar Cell. *Nano Lett.* **2010**, *10*, 5001−5005.

(5) Lu, L.; Xu, T.; Chen, W.; Lee, J. M.; Luo, Z.; Jung, I. H.; Park, H. I.; Kim, S. O.; Yu, L. The Role of N-Doped Multiwall Carbon Nanotubes in Achieving Highly Efficient Polymer Bulk Heterojunction Solar Cells. *Nano Lett.* **2013**, *13*, 2365−2369.

(6) Jung, Y.; Li, X.; Rajan, N. K.; Taylor, A. D.; Reed, M. A. Record High Efficiency Single-Walled Carbon Nanotube/Silicon p-n Junction Solar Cells. *Nano Lett.* **2013**, *13*, 95−99.

(7) Shi, E.; Li, H.; Yang, L.; Zhang, L.; Li, Z.; Li, P.; Shang, Y.; Wu, S.; Li, X.; Wei, J.; et al. Colloidal Antireflection Coating Improves Graphene-Silicon Solar Cells. *Nano Lett.* **2013**, *13*, 1776−1781.

(8) Bernardi, M.; Palummo, M.; Grossman, J. C. Semiconducting Monolayer Materials as a Tunable Platform for Excitonic Solar Cells. *ACS Nano* **2012**, *6*, 10082−10089.

(9) Lumb, M. P.; Yakes, M. K.; Gonzlez, M.; Vurgaftman, I.; Bailey, C. G.; Hoheisel, R.; Walters, R. J. Double Quantum-Well Tunnel Junctions with High Peak Tunnel Currents and Low Absorption for InP Multi-Junction Solar Cells. *Appl. Phys. Lett.* **2012**, *100*, 213907−213910.

(10) Meng, L.; Wang, D.; Li, Q.; Yi, Y.; Brédas, J.-L.; Shuai, Z. An Improved Dynamic Monte Carlo Model Coupled with Poisson Equation to Simulate the Performance of Organic Photovoltaic Devices. *J. Chem. Phys.* **2011**, *134*, 124102−124108.

(11) Meng, L.; Shang, Y.; Li, Q.; Li, Y.; Zhan, X.; Shuai, Z.; Kimber, R. G. E.; Walker, A. B. Dynamic Monte Carlo Simulation for Highly Efficient Polymer Blend Photovoltaics. *J. Phys. Chem. B* **2010**, *114*, 36−41.

(12) Qi, B.; Wang, J. Fill Factor in Organic Solar Cells. *Phys. Chem. Chem. Phys.* **2013**, *15*, 8972−8982.

(13) Koster, L. J. A.; Smits, E. C. P.; Mihailetchi, V. D.; Blom, P. W. M. Device Model for the Operation of Polymer/Fullerene Bulk Heterojunction Solar Cells. *Phys. Rev. B* **2005**, *72*, 085205−085213.

(14) Shang, Y.; Li, Q.; Meng, L.; Wang, D.; Shuai, Z. Device Simulation of Low-Band Gap Polymer Solar Cells: Influence of Electron-Hole Pair Dissociation and Decay Rates on Open-Circuit Voltage. *Appl. Phys. Lett.* **2010**, *97*, 143511−143513.

(15) Elstner, M.; Porezag, D.; Jungnickel, G.; Elsner, J.; Haugk, M.; Frauenheim, T.; Suhai, S.; Seifert, G. Self-Consistent-Charge Density-Functional Tight-Binding Method for Simulations of Complex Materials Properties. *Phys. Rev. B* **1998**, *58*, 7260−7268.

(16) Datta, S. *Electronic Transport in Mesoscopic Systems*; Cambridge University Press: Cambridge, U.K., 1997.

(17) Keldysh, L. Diagram Technique for Nonequilibrium Processes. *J. Exp. Theor. Phys.* **1965**, *20*, 1018−1027.

(18) Haug, H.; Jauho, A.-P. *Quantum Kinetics in Transport and Optics of Semiconductors*; Springer: New York, 2008.

(19) Yam, C. Y.; Peng, J.; Chen, Q.; Markov, S.; Huang, J. Z.; Wong, N.; Cho Chew, W.; Chen, G. H. A Multi-Scale Modeling of Junctionless Field-Effect Transistors. *Appl. Phys. Lett.* **2013**, *103*, 062109−062113.

(20) Marlan, O. Scully, M. S. Z. *Quantum Optics*; Cambridge University Press: Cambridge, U.K., 1997.

(21) Henrickson, L. E. Nonequilibrium Photocurrent Modeling in Resonant Tunneling Photodetectors. *J. Appl. Phys.* **2002**, *91*, 6273−6281.

(22) Stewart, D. A.; Léonard, F. Photocurrents in Nanotube Junctions. *Phys. Rev. Lett.* **2004**, *93*, 107401−107404.

(23) Zhang, Y.; Yam, C. Y.; Chen, G. H. Dissipative Time-dependent Quantum Transport Theory. *J. Chem. Phys.* **2013**, *138*, 164121−164130.

(24) Jauho, A.-P.; Wingreen, N. S.; Meir, Y. Time-Dependent Transport in Interacting and Noninteracting Resonant-Tunneling Systems. *Phys. Rev. B* **1994**, *50*, 5528−5544.

(25) Galperin, M.; Nitzan, A. Optical Properties of Current Carrying Molecular Wires. *J. Chem. Phys.* **2006**, *124*, 234709−234725.

(26) Galperin, M.; Nitzan, A. Current-Induced Light Emission and Light-Induced Current in Molecular-Tunneling Junctions. *Phys. Rev. Lett.* **2005**, *95*, 206802−206805.

(27) Mahan, G. *Many Particle Physics*; Kluwer Academic/Plenum: New York, 2000.

(28) Lake, R.; Klimeck, G.; Bowen, R. C.; Jovanovic, D. Single and Multiband Modeling of Quantum Electron Transport through Layered Semiconductor Devices. *J. Appl. Phys.* **1997**, *81*, 7845−7869.

(29) Lu, W.; Xiang, J.; Timko, B. P.; Wu, Y.; Lieber, C. M. One-Dimensional Hole Gas in Germanium/Silicon Nanowire Hetero-structures. *Proc. Natl. Acad. Sci. U.S.A.* **2005**, *102*, 10046−10051.

(30) Wu, Y.; Cui, Y.; Huynh, L.; Barrelet, C. J.; Bell, D. C.; Lieber, C. M. Controlled Growth and Structures of Molecular-Scale Silicon Nanowires. *Nano Lett.* **2004**, *4*, 433−436.

(31) Tian, B.; Kempa, T. J.; Lieber, C. M. Single Nanowire Photovoltaics. *Chem. Soc. Rev.* **2009**, *38*, 16−24.

(32) Garnett, E.; Yang, P. Light Trapping in Silicon Nanowire Solar Cells. *Nano Lett.* **2010**, *10*, 1082−1087.

(33) Wang, W.; Wu, S.; Reinhardt, K.; Lu, Y.; Chen, S. Broadband Light Absorption Enhancement in Thin-Film Silicon Solar Cells. *Nano Lett.* **2010**, *10*, 2012−2018.

(34) Kelzenberg, M. D.; Boettcher, S. W.; Petykiewicz, J. A.; Turner-Evans, D. B.; Putnam, M. C.; Warren, E. L.; Spurgeon, J. M.; Briggs, R. M.; Lewis, N. S.; Atwater, H. A. Enhanced Absorption and Carrier Collection in Si Wire Arrays for Photovoltaic Applications. *Nat. Mater.* **2010**, *9*, 239−244.

(35) Galperin, M.; Nitzan, A. Molecular Optoelectronics: the Interaction of Molecular Conduction Junctions with Light. *Phys. Chem. Chem. Phys.* **2012**, *14*, 9421−9438.

(36) Urich, A.; Unterrainer, K.; Mueller, T. Intrinsic Response Time of Graphene Photodetectors. *Nano Lett.* **2011**, *11*, 2804−2808.

(37) Xia, F.; Mueller, T.; Lin, Y.-m.; Valdes-Garcia, A.; Avouris, P. Ultrafast Graphene Photodetector. *Nat. Nanotechnol.* **2009**, *4*, 839−843.

(38) Yam, C. Y.; Meng, L.; Chen, G. H.; Chen, Q.; Wong, N. Multiscale Quantum Mechanics/Electromagnetics Simulation for Electronic Devices. *Phys. Chem. Chem. Phys.* **2011**, *13*, 14365−14369.

(39) Meng, L.; Yam, C. Y.; Koo, S.; Chen, Q.; Wong, N.; Chen, G. H. Dynamic Multiscale Quantum Mechanics/Electromagnetics Simulation Method. *J. Chem. Theory Comput.* **2012**, *8*, 1190−1199.

(40) Meng, L.; Yin, Z.; Yam, C. Y.; Koo, S.; Chen, Q.; Wong, N.; Chen, G. H. Frequency-Domain Multiscale Quantum Mechanics/Electromagnetics Simulation Method. *J. Chem. Phys.* **2013**, *139*, 244111−244116.